Beyond fixed points: transient quasi-stable dynamics emerging from ghost channels and ghost cycles

D. Koch,[a)] A. Nandan,[a)] G. Ramesan, and A. Koseska[b)]
Cellular computations and learning, Max Planck Institute for Neurobiology of Behavior – caesar, Bonn, Germany

(Dated: 2 October 2023)

Dynamical description of natural systems has generally focused on fixed points, with saddles and saddle-based phase space objects such as heteroclinic channels and heteroclinic cycles being central concepts behind the emergence of quasi-stable dynamics or long transients. Reliable and robust quasi-stable dynamics observed for real, inherently noisy systems is, however, not met by saddle-based dynamics, as demonstrated here. Generalizing the notion of ghost states, we provide a complementary framework for emergence of sequential quasi-stable dynamics that does not rely on (un)stable fixed points, but rather on slow directed flows on ghost manifolds from which *ghost channels* and *ghost cycles* are generated. Moreover, we show that these novel phase space objects are an emergent property of a broad class of models, typically used for description of natural systems.

Keywords: ghost states; he stateteroclinic channels; heteroclinic cycles; saddle fixed points; metastability; quasi-stable dynamics; slow manifolds

Living and man-made, but also ecological or climate systems are classically described to exhibit asymptotic behavior, implying that the observed dynamics is retained indefinitely in absence of a perturbation. Mathematically, such dynamics corresponds to invariant sets that represent objects in phase space, the simplest being stable fixed points that are separated by unstable fixed points or saddles (Fig. 1(a)-(c)). However, a growing body of empirical evidence suggests that real-world systems are often characterized by long transients which are quasi-stable (with anomalously slow relaxation[1,2]) with fast switching between them. The duration of the quasi-stable dynamical patterns is much larger than one would expect from the characteristic elementary processes, whereas the switching is triggered by external signals or system-autonomously, and occur on a timescale much shorter than the one of the preceding dynamical pattern. Examples include neuronal firing patterns during olfactory sensing or discrimination tasks[3–5], pattern matching during camouflage in animals[6], cellular signaling systems[7,8], ecological[9–11], as well as earth and climate systems[12,13]. Particularly in the context of neuronal systems, the described dynamics has been often referred to as *metastable*[14–16]. Some forms of these observed long transients have been conceptualized by trapping of the system's dynamics ("crawl-by") in the vicinity of a saddle[10], whereas heteroclinic objects consisting of joined saddles are thought to explain the switching between different quasi-stable dynamical patterns[17,18]. Recently, saddle-node "ghosts" have been additionally proposed to underlie transient cell signaling[7] or epigenetic memory[8], as well as regime-shifts in marine ecosystems[10].

Generalizing the concept of ghost states[1,19,20], we provide here a complementary theoretical framework that does not rely on (un)stable fixed points, but rather on transiently stable flows in phase space generated by ghost manifolds, from which *ghost channels* and *ghost cycles* can be created. The ghost manifold is represented by a very shallow slope in the quasi-potential landscape, which transiently captures the incoming trajectories, generating slow dynamics underlying quasi-stability (Fig. 1(d)). The ghost structures correspond to Lyapunov-unstable invariant set solutions which are bounded[21], enabling the dynamics to converge to specified areas in the system's state space. By defining dynamical criteria for the characterization of slow dynamics on the ghost manifolds, we demonstrate that they are more suitable than saddles and heteroclinic objects for the description of long transients and for reliable guiding of trajectories in inherently noisy systems.

Properties of ghost manifolds.—To derive and generalize the basic dynamical characteristics of ghost manifolds, let us consider a conceptual 2D-system of first order differential equations (Eq. 1): $\dot{\mathbf{x}} = \mathbf{F}(\mathbf{x})$, where $\mathbf{x} = (x, y) \in R^2$ and $\mathbf{F}(\mathbf{x}) = (f_x, f_y)$; $f_x = \alpha + x^2$, $f_y = -y$. For $\alpha < 0$, the system has a stable fixed point and a dissipative saddle (saddle value: $\nu = \frac{Re\lambda_s}{\lambda_u} \approx 1.11$), whereas for $\alpha \to 0^+$ (Supplementary Fig. 1(a)), a ghost state or a so-called bottleneck exists[20].

The phase space regions that are characterized by slow dynamics can be identified using an auxiliary scalar function $q(x) = \frac{1}{2}|\mathbf{F}(\mathbf{x})|$ that is related to the kinetic energy of the system[22]. $q(\mathbf{x}^*) = \mathbf{0}$ if and only if x^* is a fixed point of the system, whereas low kinetic energy ($q \approx 0$, identified by minimizing $|\mathbf{F}(\mathbf{x})|$) in turn corresponds to regions with slow dynamics beyond fixed points. Calculating the kinetic energy for Eq. 1 shows that q is not only minimized around the saddle fixed point (Fig. 2(a)

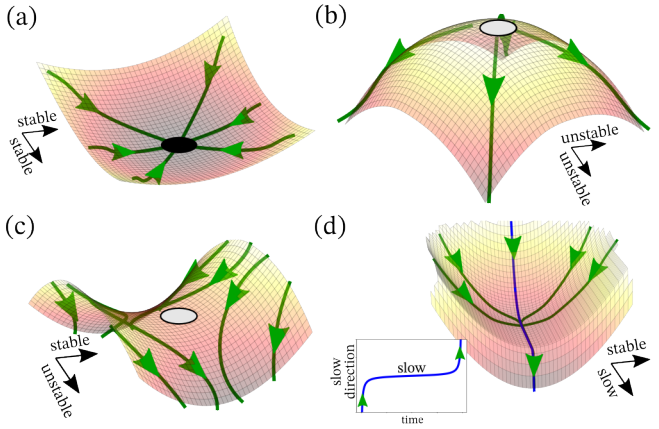

FIG. 1 Schematics of different types of phase space objects. Quasi-potential landscapes of (a) stable, (b) unstable, and (c) saddle fixed point. Black/gray dot: stable/unstable fixed point localization. (d) Quasi-potential landscape of a ghost state. Note the absence of a fixed point. Green lines: trajectories with arrows showing the direction of the flow. Inset: time course of a trajectory depicting a slow transition through the ghost manifold.

top; we omit the stable fixed point for $\alpha < 0$ for brevity), but also a region of slow dynamics exists for $\alpha \to 0^+$ (Fig. 2(b) top). In this parameter regime the system does not have a fixed point, and the slow dynamics spans across a phase space area (corresponding to the shallow slope region in Fig.1(d)). In the regions where the norm of the dynamics is close to zero ($q_{thresh} = 10^{-2}$), local linear expansion of the dynamics is still valid[22]. We thus numerically evaluated the two eigenvalues (λ^s_{max} and λ^s_{min}) in these regions using the Jacobian of Eq. 1 and found λ^s_{min} to be negative in both cases (Supplementary section I and Supplementary Fig. 1(b)). The λ^s_{max} on the other hand remained positive in the complete q_{thresh} region around the saddle, whereas a gradient of λ^s_{max} values is characteristic for the slow dynamics region when $\alpha \to 0^+$ (Fig. 2(a), (b), middle). As λ^s_{max}, λ^s_{min} determine the flow direction, trajectories starting along the stable manifold are deflected along the unstable manifold of the saddle, whereas for the ghost case, the flow in phase space transverses across the complete low kinetic energy domain (Fig. 2(a) and (b) bottom, respectively). This phase space structure of a set of orbits that are reliably funneled in a unique direction we refer to as *ghost manifold*. Moreover, a region with $\lambda^s_{max} \approx 0$ along the ghost manifold likely ensures a pronounced trapping, such that the system effectively spends longer intervals in this phase-space area, leading to the emergence of quasi-stable dynamics.

To verify the conjecture that $\lambda^s_{max} \approx 0$ induces longer trapping time, we determined both analytically and numerically the local piece-wise trapping times of the system's trajectories in the respective q_{thresh} regions as a function of the local λ^s_{max}, by explicitly integrating Eq. 1 along each of the N segments of the trajectory (segments defined with an initial $(x_{in,i}, y_{in,i})$ and final $(x_{fin,i}, y_{fin,i})$ point, Supplementary section

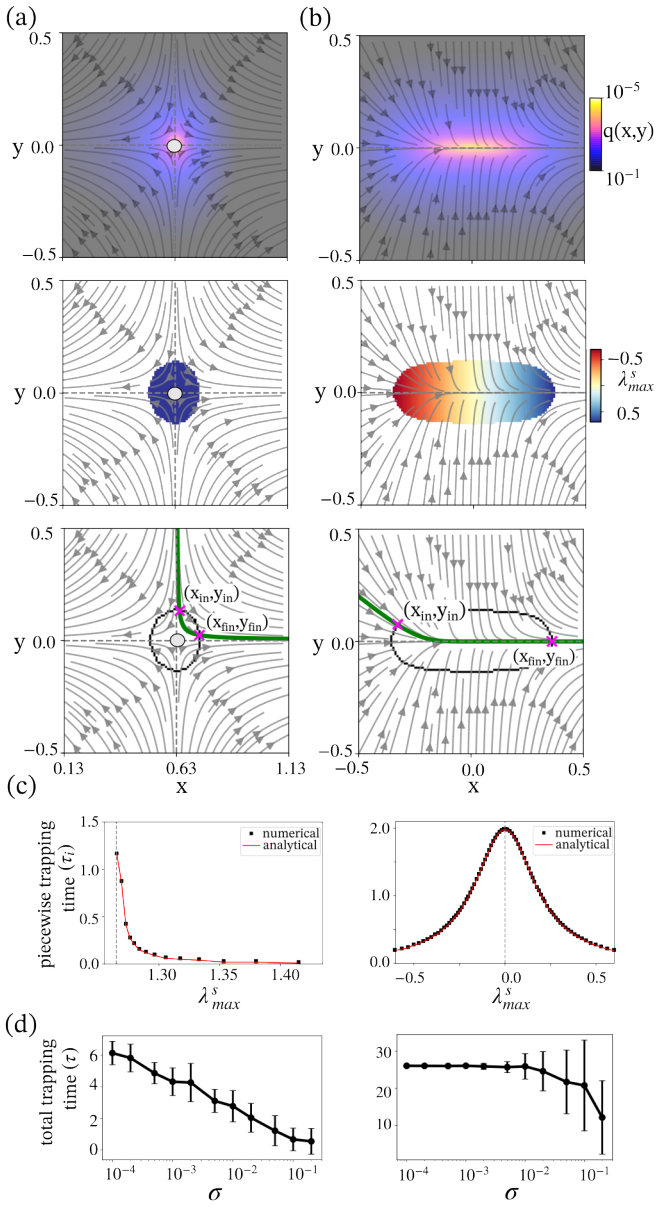

FIG. 2 Dynamical criteria for the emergence of quasi-stable transients from saddles vs. ghost manifolds. (a) Top: Kinetic energy values ($q(x, y)$) around saddle fixed point ($\alpha = -0.4$ in Eq. 1); middle: Numerically estimated maximum eigenvalue (λ^s_{max}) at the slow dynamics region ($q(x, y) < q_{thresh} = 0.01$); Bottom: evolution of an exemplary phase space trajectory in the vicinity of the saddle fixed point. Black contour: slow region. Magenta crosses: entry and exit point of the trajectory. (b) Same as in (a), but for a ghost state ($\alpha = 0.01$ in Eq. 1). In (a), (b), gray lines with arrows indicate phase space flow. (c) Analytical and numerical piece-wise trapping time (cf. Supplementary section II for details) as a function of λ^s_{max} for a trajectory that transverses across the slow dynamics regions ($q(x, y) < q_{thresh}$) of the saddle fixed point (left) and the ghost state (right). Dashed vertical line: λ^s_{max} where $q(x, y)$ is minimum. (d) Dependence of the total trapping time in the slow dynamics region of the saddle fixed point (left) and the ghost state (right) for different noise intensities σ. Mean and standard deviation from estimated from 30 different trajectories are shown. See also Supplementary Material.

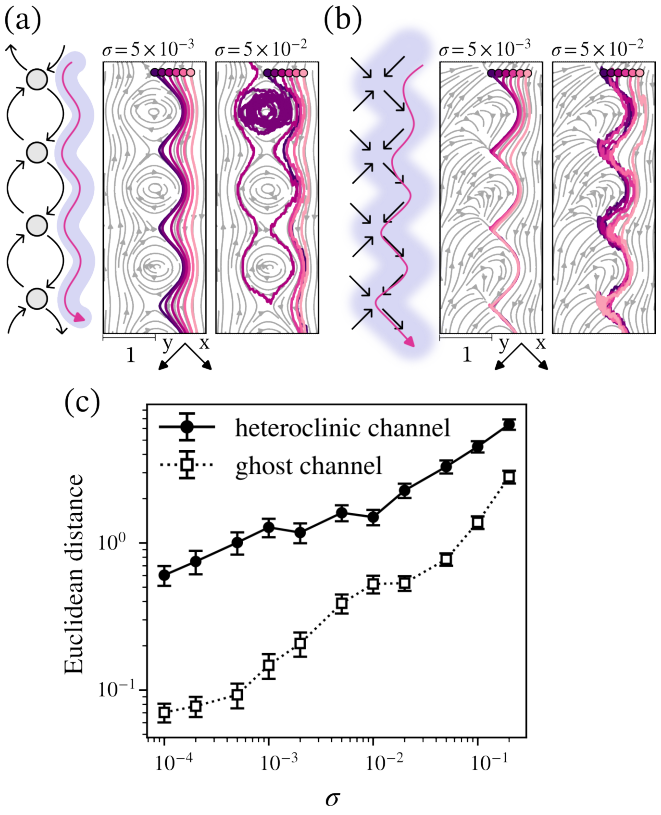

FIG. 3 Comparison of heteroclinic and ghost channels' dynamics. (a) Left: Schematic of a HCh: four saddle fixed points joined by heteroclinic connections. Right: Exemplary trajectories starting from six different initial conditions, for two different noise intensities σ. (b) Same as in (a), only for a ghost channel (GCh). (c) Euclidean distance between pairwise trajectories in the HCh or GCh as a function of σ. Mean ± SEM from 30 trajectories is shown.

II). The functional forms of the analytical expressions $\tau_{i,saddle} = \frac{1}{\lambda^s_{max}}(\ln|\frac{x_{fin,i}-\lambda^s_{max}/2}{x_{fin,i}+\lambda^s_{max}/2}|-\ln|\frac{x_{in,i}-\lambda^s_{max}/2}{x_{in,i}+\lambda^s_{max}/2}|)$, and $\tau_{i,ghost} = \frac{2}{\lambda^s_{max}}(\tan^{-1}(\frac{2x_{fin,i}}{\lambda^s_{max}}) - \tan^{-1}(\frac{2x_{in,i}}{\lambda^s_{max}}))$ show that the piece-wise trapping time quickly decays along positive λ^s_{max} for the saddle, whereas for the ghost-manifold, a parabolic dependency on the gradient of λ^s_{max} applies (corroborated by numerical simulations, Fig. 2 (c)). Any trajectory approaching the saddle can pass only through one quadrant of the low-kinetic energy domain. In the case of the ghost manifold however, the trajectories pass along the full length of the low-kinetic energy domain. Thus, the total trapping time on the saddle compared to the ghost manifold show an order of magnitude difference (in the presence of low noise intensity $\sigma = 10^{-4}$, Fig.2(d)). Moreover, the total trapping time on the saddle decreases strictly monotonically with increasing σ, whereas for the ghost manifold it is constant over large σ range, decaying to half-maximum only at $\sigma \sim 10^{-1}$. This robustness of the total trapping time, even under high intrinsic noise for the ghost (and thereby the emergence of reliable quasi-stable dynamics), directly results from the geometry of the manifold: the ghost has only a single unstable direction along which the system can escape the low-kinetic energy domain, whereas the saddle features two unstable directions resulting in decreased stability with increasing σ. These features are not a peculiarity of the given model, but generic for ghost manifolds (Supplementary Fig. 1(e)).

Ghost channels and ghost cycles.—The empirically observed sequential quasi-stable dynamics has been so far described to occur from heteroclinic objects, where the unstable manifold of the preceding saddle represents a stable manifold for the next in the sequence. Considering the lack of fidelity of single saddles in presence of noise, we hypothesized that the observed real-world dynamics could instead emerge from a novel type of phase-space objects based on ghost manifolds. In analogy to heteroclinic objects, we term these objects *ghost channels* and *ghost cycles*. Similarly to heteroclinic channels (HCh) (Fig. 3(a), left), we construct ghost channels (GCh) by aligning ghost manifolds such that the unique unstable direction of the preceding ghost is the stable direction for the following one (Fig. 3(b), left). Numerical simulations showed that the reproducibility of the HCh dynamics is compromised for increasing noise intensity, as the trajectories stochastically exit the channel along the unstable manifold of the saddles (eventually getting trapped in the nearby attractors, Fig. 3(a), right; Supplementary Fig. 2(a,b)). Thus, quasi-stable sequential dynamics cannot be guarantied for the HCh. In contrast, the GCh uniquely funnels the system's trajectories in phase space even for increased noise intensity (Fig. 3(b) and Fig. 2(c,d)), as corroborated by low Euclidean distance ($ED < 1$) among them, even for $\sigma \leq 10^{-1}$ (Fig. 3(c)). This suggests that GCh guaranty reproducible quasi-stable sequential switching dynamics, in contrast to the HCh. Ghost channels are an emergent property of a broad class of systems including low-dimensional systems in a parametric vicinity of aligned saddle-node bifurcations, or sequentially coupled network modules as typical for signal transduction systems in cells (Supplementary Fig. 2(e) and section III.C).

To conceptualize the emergence of transiently stable sequential oscillatory dynamics, we next construct ghost cycles (GC; Fig.4(e)) and characterize their dynamics in comparison to heteroclinic cycles (HC; Fig.4(a)). We set the trapping times (in arbitrary units) along a single saddle and ghost to be similar at low noise intensity by adjusting the saddle-values of a generic noise-driven Lotka-Volterra HC model (Supplementary Fig. 3). The period of the HC[23], $T \sim |ln\sigma|/\lambda_u$ decreases almost exponentially as the noise intensity is increased, as higher σ causes a decrease of the total trapping time at the saddle fixed points (Fig. 4(b), (d)). Moreover, the intervals in which the system's dynamics spends switching between the saddles within one HC period dominates even for intermediate noise intensities ($\sigma \leqslant 10^{-3}$). Generally, to maintain the trajectory of the system within the heteroclinic cycle, the system's variables have to be restricted to positive values[24]. However, during the noise-induced switching, the system's trajectories increasingly

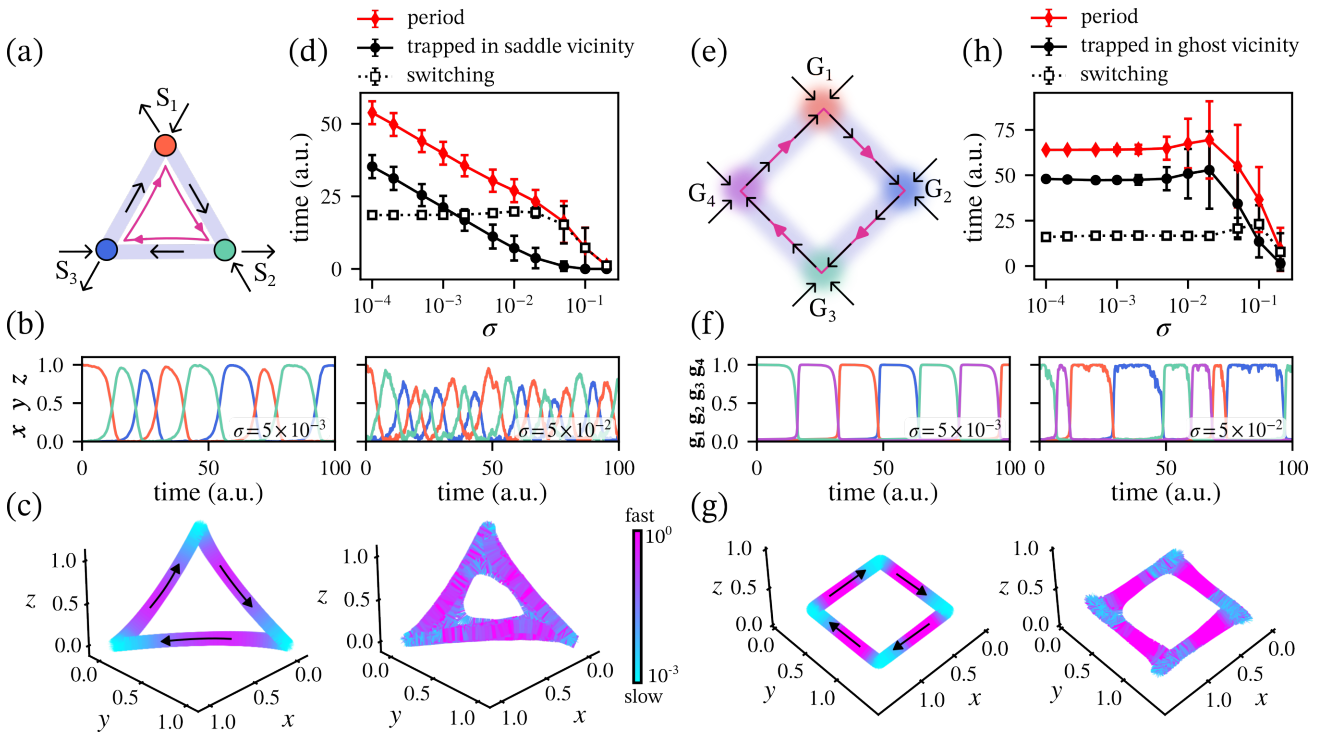

FIG. 4 Comparison of dynamical characteristics of heteroclinic and ghost cycles. Schematic (a) and exemplary time series (b) of a heteroclinic cycle for two different noise intensities σ. (c) Exemplary phase space trajectories with color-coded velocity for the same noise intensities as in (b). (d) Characteristic HC times as a function of σ: HC period (red), total trapping time at the saddles (solid black) and switching time (dashed black line) are shown. Vicinity was determined by three-dimensional spheres of radius $\epsilon = 0.1$ centered around the saddles. The mean $\pm$ root mean squared error of the standard deviation over time is plotted from 30 trajectories. (e, f, g) Same as in (a, b, c), only for a ghost cycle. In (g), color bar as in (c). (h) Characteristic GC times as a function of σ. Labeling and quantification equivalent to (d).

fill phase-space regions distant to the heteroclinic backbone. Consistently, the speed of the trajectory in phase space, an indicator of how long the trajectory spends in distinct phase space regions, shows that the separation of slow dynamics in the saddle vicinity and fast switching between saddles is diminished for increased noise intensity (Fig. 4(c)). These results therefore indicate that the ability of HCs to serve as a basis for quasi-stable oscillatory dynamics with rapid sequential switching is strongly compromised in the presence of noise. In contrast, increasing noise intensity does not affect the mean period of the GC over a large range of noise levels and the trajectories stay bounded along the cycle (Fig. 4(f-h)). The times spent on the ghosts along the cycle remain more than 2 fold larger than the transition times between the ghosts, even for $\sigma > 10^{-2}$. This is also reflected in the speed of the trajectory in phase space: the slow dynamics at the ghosts and fast switching between them are preserved even under the influence of high noise (Fig. 4(g)). These results therefore demonstrate that GCs provide the dynamical basis for description of quasi-stable dynamical patterns with rapid switching among them that is frequently observed in real-world systems. Generally, GCs can occur when a limit cycle terminates via a single or multiple simultaneous Saddle Nodes on Invariant Cycle (or SNIC) bifurcations[25–28]. Bifurcation analysis of the GC model indeed shows that decreasing α leads to switching from stable steady state to stable limit cycle oscillations (via a Hopf bifurcation), which is terminated via 4 SNICs (Supplementary Fig. 4(a-c)). In the vicinity of the SNICs, the dynamics of the system is governed by the SNs that are about to emerge: after being transiently trapped on a ghost manifold, the system escapes this state just to be trapped by the next one, thus continually switching between the ghost manifolds in the sequence. Equivalent quantitative changes in the dynamics, and thus emergence of a GC is also observed e.g. for generic gene regulatory network models proposed to underlie stem cell differentiation[27] (Supplementary Fig. 4(d-f)) or anterior-posterior patterning in metazoans[26].

Chimeric ghost/saddle structures.—Real-world data, especially one from neuronal recordings during cognitive tasks or distinct behavioral sequences[29,30], shows that the system's components not only have quasi-stable dynamics, but also selectively explore distinct phase space areas. This dynamics is usually described by low-dimensional manifolds characterised by interconnecting loops from which other branches bifurcate or rejoin[31]. We propose here that minimal phase space objects giving rise to such behavior could likely be chimeras of saddles and ghost, as exemplified in Fig.5(a). The ghost cycles endow the system with slow dynamics giving rise

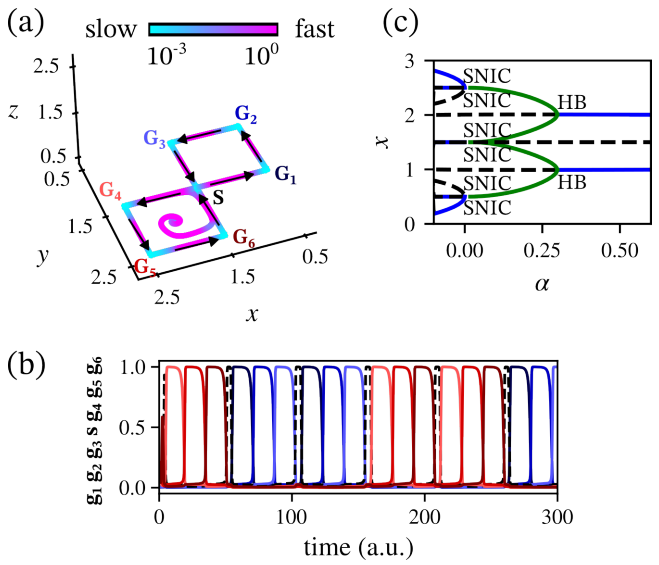

FIG. 5 (a) Chimeric phase-space object consisting of two ghost cycles joined by a saddle fixed point (s). (b) Time courses of the chimeric structure for $\sigma = 10^{-4}$. (c) Bifurcation diagram depicting the dynamic mechanism by which the phase-space object emerges for $\alpha \approx 0^{+}$, in the vicinity of the SNIC (saddle-node on invariant cycle bifurcation). Blue/green lines: stable spiral fixed points/limit cycles; dashed lines: unstable saddle fixed point. HB: Andronov-Hopf bifurcation.

to quasi-stable sequential oscillatory patterns (Fig.5(b)), whereas the saddle fixed point at the junction enables noise-induced alternating between the GCs ($\sigma = 10^{-4}$). The dynamic mechanism by which this chimeric phase space object emerges is generic as depicted by the bifurcation diagram Fig.5 (c), and thus likely to emerge in a broad class of systems.

Conclusions and outlook.—In summary, we have introduced the concepts of ghost channels and cycles as novel phase space objects that reliably give rise to sequential quasi-stable dynamical patterns with a fast switching among them. Such dynamics has been experimentally observed for neuronal activity during behavioral or cognitive tasks[29–31], olfactory processing[3], ecological systems[10] etc. The quantification of the time spent on the ghost manifold in comparison to that for a saddle demonstrates that ghosts provide robust trapping of the system's dynamics and thereby reliable quasi-stability of the dynamical pattern in the presence of noise. This emerges from slow dynamics of the system which spans a larger region in phase space, characterized by a gradient of eigenvalues that passes through zero. Effectively, the emergence of a slow time scale is related to the closeness to a bifurcation point - a parametric region where the nullclines of the system do not intersect, but are close to each other. Given that the ghost manifold that emerges has a single unstable direction (in contrast to an unstable dimension for the saddle), the dynamics of the system is not organized by fixed points, but rather a continuous flow in phase space that is uniquely guided, providing robustness to the system. However, to generate context-dependent dynamics, alternating the flow direction in phase space can be achieved with the presence of a saddle, as we have demonstrated. We therefore suggest that these chimeric phase-space objects, in contrast to the heteroclinic concept[32], can potentially give a mechanistic understanding how the dynamics along the manifold arises for neuronal activity or behavioral data[6,29]. It would be therefore of interest to investigate whether the alternating dynamics can be reliably controlled given defined time-dependent input signals, and to which extent these chimeric structures can be used for computation. Moreover, the presence of distinct time-scales can provide a novel direction for development of time-series analysis methods for detecting quasi-stable patterns and corresponding transitions, e.g. via phase-space based metrics[33]. We propose that this conceptual framework will provide new perspectives on natural systems where long transients are typical.

A.K. acknowledges funding by the Max Planck Society via the Lise Meitner Excellence Programme. The authors thank A. Aulehla and K. Lehnertz for valuable feedback on the manuscript, and J. Gunawardena and J. Garcia-Ojalvo for insightful discussions.

SUPPLEMENTARY MATERIALS

I. NUMERICAL ESTIMATION OF EIGENVALUE SPECTRUM AT PHASE SPACE REGION OF SLOW DYNAMICS

Generally, in the regions where the norm of the dynamics is close to zero ($q(\mathbf{x}) < q_{thresh}$), local linear expansion of the dynamics is still valid. When linearizing around a slow point, $\mathbf{x^s}$, the local linear system takes the form,

$$\frac{\mathbf{d}\delta\mathbf{x}}{dt} = \mathbf{F}(\mathbf{x^s}) + \mathbf{F'}(\mathbf{x^s})\delta\mathbf{x} \tag{1}$$

where $\mathbf{F'}(\mathbf{x^s})$ is the Jacobian of the system evaluated at the slow point, and $\delta\mathbf{x}$ is the perturbation added to $\mathbf{x^s}$. In practice, it can be considered that the constant term $\mathbf{F}(\mathbf{x^s})$ is negligible, therefore it can be set to zero[22]. This enables to estimate the eigenvalues of $\mathbf{F'}(\mathbf{x^s})$, λ^s_{min} and λ^s_{max} as in classical linear stability analysis[20], and approximate the local dynamics of the slow points using the manifolds shaped by these eigenvalues.

II. ANALYTICAL DESCRIPTION OF TRAPPING TIME AT GHOST/SADDLE STATES

In order to find the dependence between the trapping time at the ghost state and the eigenvalues, let us consider the normal form of the saddle-node bifurcation in Eq. 1. The equations has steady states for $x^* = \pm\sqrt{-\alpha}$, and a saddle-node bifurcation at $\alpha = 0$. The Jacobian of the system is given by,

$$J = \begin{bmatrix} 2x^* & 0 \\ 0 & -1 \end{bmatrix} \quad (2)$$

with eigenvalues $\lambda_{min} = -1$ and $\lambda_{max} = 2x^*$ (Supplementary Fig. 1(a), (b) and Fig. 1 (a), (b)).

Since Eq.1 is explicitly integrable, the time of flight of the trajectory $\tau(\alpha)$ from an initial (x_{in}, y_{in}) to a final point (x_{fin}, y_{fin}) is given by,

$$\begin{aligned} \tau(\alpha) &= \int_{x_{in}}^{x_{fin}} \frac{1}{dx/dt}\, dx \\ &= \int_{x_{in}}^{x_{fin}} \frac{1}{\alpha + x^2}\, dx \end{aligned} \quad (3)$$

For $\alpha < 0$ (where the saddle and the stable fixed point co-exist) this integral is given by,

$$\begin{aligned} \tau(\alpha) &= \int_{x_{in}}^{x_{fin}} \frac{1}{-|\alpha| + x^2}\, dx \\ &= \frac{1}{2\sqrt{|\alpha|}}(ln|\frac{x_{fin} - \sqrt{|\alpha|}}{x_{fin} + \sqrt{|\alpha|}}| - ln|\frac{x_{in} - \sqrt{|\alpha|}}{x_{in} - \sqrt{|\alpha|}}|) \end{aligned} \quad (4)$$

where $|\alpha|$ denotes the absolute value of α, whereas for $\alpha > 0$ the integral is given by:

$$\begin{aligned} \tau(\alpha) &= \int_{x_{in}}^{x_{fin}} \frac{1}{\alpha + x^2}\, dx \\ &= \frac{1}{\sqrt{\alpha}}(tan^{-1}(\frac{x_{fin}}{\sqrt{\alpha}}) - tan^{-1}(\frac{x_{in}}{\sqrt{\alpha}})) \end{aligned} \quad (5)$$

Since the ghost state exists for $\alpha \to 0^+$, the total trapping time along the trajectory in the region of slow points can be analytically estimated as a sum of piece-wise trapping times estimated by integrating along each of the trajectory's segments (the trajectory is divided into N segments of length $2\omega = 0.01$, Supplementary Fig. 1(c)):

$$\tau_i(\alpha) = \frac{1}{\sqrt{\alpha}}(tan^{-1}(\frac{x_{fin,i}}{\sqrt{\alpha}}) - tan^{-1}(\frac{x_{in,i}}{\sqrt{\alpha}})) \quad (6)$$

where $i \in [0, N]$ denotes the i^{th} piece of trajectory between $x_{in,i}, x_{fin,i}$ with $x_{in,0} = x_{in}$, $x_{fin,N} = x_{fin}$ for the boundary segments and $x_{in,i} = x_{fin,(i-1)}$ for the rest. The total trapping time is then given by $\sum_{i=1}^{N} \tau_i(\alpha) = \tau(\alpha)$.

Let us consider a fictitious fixed point $(x^f, y^f) = (\sqrt{\alpha}, 0)$ which is a reflection of the saddle fixed point that disappeared at $\alpha = 0$. In the vicinity of the bifurcation this fictitious fixed point satisfies the criteria of a slow point $(q(x^f, y^f) < q_{thresh})$, hence the local eigenvalue along the ghost manifold can be approximated to be $\lambda^s_{max} = \lambda^i_{max} = 2\sqrt{\alpha}$. Using this relation, an expression of τ_i as a function of the eigenvalue λ^i_{max} is given by:

$$\tau_i(\lambda^i_{max}) = \frac{2}{\lambda^i_{max}}(tan^{-1}(\frac{2x_{fin,i}}{\lambda^i_{max}}) - tan^{-1}(\frac{2x_{in,i}}{\lambda^i_{max}})) \quad (7)$$

Numerical and analytical dependence is shown in Fig. 2(c). Given that the trapping time is a local quantity, the approximation is valid only for small w ($x_{fin,i} \approx x_{in,i}$).

Similarly, from Eq. (4) the piecewise trapping time around the saddle fixed point is given by"

$$\begin{aligned} &\tau_i(\lambda^i_{max}) = \\ &\qquad \frac{1}{\lambda^i_{max}}(ln|\frac{2x_{fin,i} - \lambda^i_{max}}{2x_{fin,i} + \lambda^i_{max}}| - ln|\frac{2x_{in,i} - \lambda^i_{max}}{2x_{in,i} - \lambda^i_{max}}|) \end{aligned} \quad (8)$$

III. MODEL EQUATIONS AND PARAMETERS

III.A. Supplementary example of a ghost model

To examine the dynamical features of ghost state, we have additionally analyzed a single ghost model described by Sussillo et al.[22]:

$$\begin{aligned} \dot{x} &= y - (x^2 + \frac{1}{4} + \alpha); \\ \dot{y} &= x - y \end{aligned} \quad (9)$$

The ghost state is observed for $\alpha = 0.001$, and the dependence of the total trapping time on the ghost vs. the noise intensity σ is shown in Supplementary Fig. 1(e).

III.B. Construction of generic heteroclinic/ghost channels (HCh/GCh), heteroclinic/ghost cycles (HC/GC) and mixed ghost/saddle networks

To define ghost channels/cycles as phase space objects, we used a generic, geometric modeling approach to define the flow in an abstract 2D/3D phase space, following the method described by Morrison & Young[32] (a similar approach has been used in[34]). For this, the phase space is partitioned into $1 \leq i \leq k$ distinct areas or volumes, and for each area or volume, a function f_i defines specific dynamics in each partition (e.g. ghost, saddle, uniform flow etc.). The full system's dynamics is thus given by $\frac{d}{dt}\mathbf{x} = \sum_{\mathbf{i=1}}^{\mathbf{n}} \mathbf{w_i}(\mathbf{x})\mathbf{f}(\mathbf{x})$, and $w_i(\mathbf{x})$ assigns a high weight to f_i if and only if $\mathbf{x}$ is within the i^{th} partition of the phase space, to ensure a unique dynamics. Specifically, partitions of the phase space are given by cubes defined by coordinates x_i^{min},x_i^{max},y_i^{min}, y_i^{max}, z_i^{min} and z_i^{max} and weighting functions by

$$\begin{aligned} w_i(\mathbf{x}) = \frac{\mathbf{1}}{\mathbf{4}} &(tanh(\gamma(x - x_i^{min})) - tanh(\gamma(x - x_i^{max}))) \\ &\times(tanh(\gamma(y - y_i^{min})) - tanh(\gamma(y - y_i^{max}))) \\ &\times(tanh(\gamma(z - z_i^{min})) - tanh(\gamma(z - z_i^{max}))), \end{aligned}$$

where $\mathbf{x} = (\mathbf{x}, \mathbf{y}, \mathbf{z})^{\mathbf{T}}$ and γ defines how steep the transitions in the weighting functions between partitions are. Generally, the dynamics within a partition is defined by $f(\mathbf{x}) = (\hat{\mathbf{f}}(\mathbf{x}), \hat{\mathbf{g}}(\mathbf{y}), \hat{\mathbf{h}}(\mathbf{z}))$, where $\hat{h}(z) = -(z - 0.5)$. For ghosts dynamics, $\hat{f}$ is given by $x \mapsto c_i(\alpha+(x-x_{offset})^2)$, $c_i \in (-1, 1)$, and $\hat{g}(y)$ by $y \mapsto \tilde{c_i}(y - y_{offset})$, $\tilde{c_i} \in (-1, 1)$, or vice versa. The offset defines the center of the partition. In both functions, c and $\tilde{c}$ were chosen to funnel the flow from three directions on the x/y plane. Saddle dynamics is defined by $\hat{f}(x)$ given by $x \mapsto -\nu(x - x_{offset}))$ defining the stable manifold, and $\hat{g}(y)$ by $x \mapsto (y - y_{offset})$ defining the unstable manifold, or vice versa. ν is the saddle value. The uniform flow is defined by $\hat{f}(x) = m_1$, $\hat{g}(y) = m_2$, $m_1, m_2 \in \mathbb{R}$. For 2D systems, the z dimension (and thus $\hat{h}$) was omitted.

To construct a heteroclinic channel in 2D, $\mathbf{f_i}$s and $\mathbf{w_i}$s were chosen such that four saddles are positioned within partitions on a diagonal and the flow on the neighbouring partitions was defined to be uniform (Fig. 3(a) and Supplementary Fig. 2(a)). To construct a ghost channel in 2D,$\mathbf{f_i}$s and $\mathbf{w_i}$s were chosen such that the unique unstable direction of the preceding ghost is a stable direction for the following ghost in the sequence (Fig. 3(b) and Supplementary Fig. 2(b)). For a ghost cycle, the repelling direction of the last ghost in the sequence is an attracting direction of the first ghost (Fig. 4(e)). Similarly, the chimeric saddle and ghost structure (Fig. 5) was generated by connecting the unstable manifold of a saddle with the attracting direction of a ghost or by connecting the repelling direction of a ghost with the stable manifold of a saddle. The full set of equations and parameters for these systems can be found in the `Python` and `XPPAUT`[35] code accompanying this article.

To obtain similar shape of the ghost cycle oscillations (Supplementary Fig. 3(a)) to that of the heteroclinic cycle oscillations (cf. equation 13 and Fig. 4(a,b)), a Euclidean distance of each point in the trajectory to each of the ghost position was obtained ($d_j = ||\overline{x} - G_j||, 1 \leq j \leq 4$,, Supplementary Fig. 3(b) left), and the corresponding distance time series (Supplementary Fig. 3(b), right) were mapped using a Hill-type function $\theta\ \Theta(d) = d^{-3}/(d^{-3} + 0.3^{-3})$ (Supplementary Fig. 3(c)). This ensures that the shape of the oscillations in the ghost cycle are comparable to those in the heteroclinic cycle. To construct HC and GC that have comparable trapping time on the saddles/ghosts, the saddle value was set to $\nu = 4$ to adjust the differences of the average time spent in saddle/ghost vicinity (colored triangles) to ¡ 1% for the lowest noise level used in this work ($\sigma = 10^{-4}$, Supplementary Fig. 3(d).

To quantify the robustness of the trajectories within the heteroclinic and ghost channels, we estimated the Euclidean distance (ED) between pairs of trajectories from different realizations of stochastic simulations: $ED = \sqrt{((x_2(t)-x_1(t))^2+(y_2(t)-y_1(t))^2)}$, where $1, 2$ represent trajectory pairs. To avoid effects from different trapping times on the ghosts/saddles, the trajectories were initially time warped using the `dtaidistance` package (v 2.3.9) in `Python`. The average ED over time from 30 replicates (mean ± root mean squared error of the standard deviation over time) is shown in Fig. 3(c).

III.C. Supplementary examples of ghost channels

An infinite number of saddle-node bifurcations at the same parameter value can be constructed using a periodic function such as sin or cos. Parameterizing such a system in the vicinity of the SN bifurcation results in a ghost channel. One realization of such a GCh is given by:

$$\begin{aligned} \dot{x} &= \alpha - sin(kx) \\ \dot{y} &= x - y \end{aligned} \tag{10}$$

For $k = 1$ and α=1.01, infinite number of ghost states in a sequence are observed. Phase space with numerical λ^s_{max} estimation at the regions of slow dynamics and corresponding time series are shown in Supplementary Fig. 2(e).

We next considered a biochemical network motif with double negative feedback model from Dey et al.[36], which has been re-parameterized to obtain a GCh that visits two ghost states and a stable attractor in a sequence:

$$\begin{aligned} \dot{x} &= G_x(S, y) - k_x x \\ \dot{y} &= G_y(x, y) - k_y y \\ G_x(S, y) &= g_{x,0} H^-(S) H_1^-(y) + g_{x,S} H^+(S) H_1^-(y) \\ &\quad + g_{x,y} H^-(S) H_1^+(y) + g_{x,y,S} H^+(S) H_1^+(y) \\ G_y(y, x) &= g_{y,0} H^-(x) H_2^-(y) P_R + g_{y,y} H^-(x) H_2^+(y) \\ &\quad + g_{y,x} H^+(x) H_2^-(y) P_R + g_{y,xy} H^+(x) H_2^+(y) P_R \\ H^-(S) &= \frac{1}{1 + \left(\frac{S}{S_{x,0} k_0}\right)^{n_{S,x}}} \\ H^+(S) &= 1 - H^-(S) \\ H_1^-(y) &= \frac{1}{1 + \left(\frac{y}{y_{x,0}}\right)^{n_{y,x}}} \\ H_1^+(y) &= 1 - H_1^-(y) \\ H^-(x) &= \frac{1}{1 + \left(\frac{x}{x_{y,0}}\right)^{n_{x,y}}} \\ H^+(x) &= 1 - H^-(x) \\ H_2^-(y) &= \frac{1}{1 + \left(\frac{y}{y_{y,0}}\right)^{n_{y,y}}} \\ H_2^+(y) &= 1 - H_2^-(y) \end{aligned} \tag{11}$$

where $S = 1.835$, $g_{x,0} = 4.0$, $g_{x,S} = 18.0$, $g_{A,y} = 0.7$, $g_{x,y,S} = 4.0$, $g_{y,0} = 7.5$, $g_{y,y} = 39.0$, $g_{y,x} = 1.0$, $g_{y,xy} = 7.5$, $S_{x,0} = 140$ $B_{x,0} = 315$, $x_{y,0} = 130$, $y_{y,0} = 75$, $n_{S,x} = 2.0$, $n_{y,x} = 4.0$,$n_{x,y} = 5.0$, $n_{y,y} = 6.0$, $k_x = 0.05$, $k_y = 0.075$, $P_R = 1$, and $k_0 = 0.01$.

Phase space with numerical λ^s_{max} estimation at the regions of slow dynamics and corresponding time series are shown in Supplementary Fig. 2(e) middle.

As a third example, we adapted a biochemical model from Ferrel *et al.*[37] to construct a GCh by undirectionally coupling two biochemical modules:

$$\begin{aligned}\dot{x} &= \left(k_1 S + \frac{k_2 x^n}{(K^n + x^n))}\right)(x_{tot} - x) - k_3 x \\ \dot{y} &= \left((k_1 x + \frac{k_2 y^n}{(K^n + y^n))}\right)(x_{tot} - y) - k_3 y\end{aligned} \tag{12}$$

For $S = 0, x_{tot} = 1, k_1 = 1, k_2 = 2, k_3 = 1$,
$K = 0.505, n = 4$, the model has two ghost states in a sequence (ghost channel) followed by a stable fixed point. The corresponding phase space with the numerical λ^s_{max} estimation at the regions of slow dynamics, and the time series are shown in Supplementary Fig. 2(e) right.

III.D. Model of a heteroclinic cycle

To model heteroclinic cycle dynamics, we used the 3D HC described by Horchler *et al.*[24]:

$$\frac{d}{dt}\mathbf{x} = \dot{\mathbf{x}}(\alpha - \rho\mathbf{x}), \tag{13}$$

where $\mathbf{x} = (x, y, z)^T$, $\alpha = (\alpha_1, \alpha_2, \alpha_3)$,

$$\rho = \begin{bmatrix} \alpha_1/\beta_1 & (\alpha_1 + \alpha_2)/\beta_2 & (\alpha_1 - \frac{\alpha_3}{\nu_3})/\beta_3 \\ (\alpha_2 - \frac{\alpha_1}{\nu_1})/\beta_1 & \alpha_2/\beta_2 & (\alpha_2 + \alpha_3)/\beta_3 \\ (\alpha_3 + \alpha_1)/\beta_1 & (\alpha_3 - \frac{\alpha_2}{\nu_2})/\beta_2 & \alpha_3/\beta_3 \end{bmatrix},$$

$\alpha_i = 2, \beta_i = 1$ and $\nu_i = 4$, for $i = 1, ..3$.

III.E. Supplementary example of a ghost cycle

We analyzed additionally a genetic network model described in[27]:

$$\begin{aligned}\dot{x} &= b + \frac{g}{(1 + \alpha(y^h))(1 + \beta(z^h))} - dx \\ \dot{y} &= b + \frac{g}{(1 + \alpha(z^h))(1 + \beta(x^h))} - dy \\ \dot{z} &= b + \frac{g}{(1 + \alpha(x^h))(1 + \beta(y^h))} - dz\end{aligned} \tag{14}$$

For $\alpha = 9$, $\beta = 0.1$, $h = 3$, $d = 0.2$, $b = 10^{-5}$ and $g = 1.51$, the limit cycle oscillations terminate at three SNIC bifurcations (Supplementary Fig. 4(d)). For organization before the SNIC, the behavior of the system is guided by the three SN that are about to appear, effectively displaying ghost cycle oscillations. The bifurcation diagram, the phase trajectories (colour-coded by the speed) for different parameter values, as well as the emergence of a stable fixed point and a saddle right after the SNIC bifurcation are shown in Supplementary Fig. 4(d)-(f).

IV. MODEL IMPLEMENTATION, NUMERICAL INTEGRATION AND FEATURES CHARACTERIZATION

The ODE models (Figs. 2(c), Supplementary Figs. 1(d), 2(e), 3, 4) were integrated using the 4th order Runge-Kutta scheme implemented using custom-made *Python* code. The contribution of the noise (Figs. 2(d), 3, 4 and 5, Supplementary Figs. 1(e), 2 (a-d)) is modeled as a Wiener process where Gaussian white noise is introduced as an additive term at each time step. This results in a stochastic differential equation (SDE) in Ito form, $\dot{X(t)} = f(X(t), t)dt + \sigma(t)dW(t)$, where dt denotes the step size (0.05 or 0.01 were used throughout this study), where $\sigma(t)$ describes the additive noise and $W(t)$ denotes a Wiener process whose independent increments follow a normal distribution $\sqrt{dt}N(\mu = 0, var = 1)$. For simulation of stable heteroclinic cycles, integration of the system was performed by restricting $\mathbf{x}$ to $\mathbb{R}^{\geq 0}$ as described in[24], to avoid escaping from the heteroclinic cycle via the unstable directions. The velocity of the trajectories in phase space (Figs. 4, 5 and Supplementary Fig. 4) was normalized between the 5-95 percentile of the velocity values along the trajectories for the different noise intensities form the SC and the GC independently.

[a] Equally contributing authors
[b] Electronic mail: aneta.koseska@mpinb.mpg.de

[1] A. N. Gorban, "Singularities of transition processes in dynamical systems: Qualitative theory of critical delays," Electronic Journal of Differential Equations **1**, 05 (2004).
[2] T. B. Francis, K. C. Abbott, K. Cuddington, G. Gellner, A. Hastings, Y.-C. Lai, A. Morozov, S. Petrovskii, and M. L. Zeeman, "Management implications of long transients in ecological systems," Nature Ecology and Evolution **5**, 285–294 (2021).
[3] O. Mazor and G. Laurent, "Transient dynamics versus fixed points in odor representations by locust antennal lobe projection neurons," Neuron **48**, 661–673 (2005).
[4] D. Benozzo, G. L. Camera, and A. Genovesio, "Slower prefrontal metastable dynamics during deliberation predicts error trials in a distance discrimination task," Cell Reports **35**, 108934 (2021).
[5] S. Recanatesi, U. Pereira-Obilinovic, M. Murakami, Z. Mainen, and L. Mazzucato, "Metastable attractors explain the variable timing of stable behavioral action sequences," Neuron **110**, 139–153.e9 (2022).
[6] T. Woo, X. Liang, D. A. Evans, O. Fernandez, F. Kretschmer, S. Reiter, and G. Laurent, "The dynamics of pattern matching in camouflaging cuttlefish," Nature **619**, 122–128 (2023).
[7] A. Nandan, A. Das, R. Lott, and A. Koseska, "Cells use molecular working memory to navigate in changing chemoattractant fields," eLife **11** (2022), 10.7554/elife.76825.
[8] O. Karin, E. A. Miska, and B. D. Simons, "Epigenetic inheritance of gene silencing is maintained by a self-tuning mechanism based on resource competition," Cell Systems **14**, 24–40.e11 (2023).
[9] R. M. May and W. J. Leonard, "Nonlinear aspects of competition between three species," SIAM Journal on Applied Mathematics **29**, 243–253 (1975).
[10] A. Hastings, K. C. Abbott, K. Cuddington, T. Francis, G. Gellner, Y.-C. Lai, A. Morozov, S. Petrovskii, K. Scranton, and M. L. Zeeman, "Transient phenomena in ecology," Science **361** (2018), 10.1126/science.aat6412.
[11] C. Bieg, H. Vallès, A. Tewfik, B. E. Lapointe, and K. S. McCann, "Towards a multi-stressor theory for coral reefs in a changing world," (2022), 10.1101/2022.03.22.485402.
[12] A. C. de Verdière, "A simple model of millennial oscillations of the thermohaline circulation," Journal of Physical Oceanography **37**, 1142–1155 (2007).

[13]B. Kaszás, T. Haszpra, and M. Herein, "The snowball earth transition in a climate model with drifting parameters: Splitting of the snapshot attractor," Chaos: An Interdisciplinary Journal of Nonlinear Science **29** (2019), 10.1063/1.5108837.
[14]J. A. S. Kelso, "Multistability and metastability: understanding dynamic coordination in the brain," Philos Trans R Soc Lond B Biol Sci. **367**, 906–918 (2012).
[15]G. Deco and M. Kringelbach, "Metastability and coherence: extending the communication through coherence hypothesis using a whole-brain computational perspective," Trends Neurosci. **39**, 432 (2016).
[16]K. L. Rossi, R. C. Budzinski, E. S. Medeiros, B. R. R. Boaretto, L. Muller, and U. Feudel, "A unified framework of metastability in neuroscience," arXiv:2305.05328 (2023).
[17]M. Rabinovich, A. Volkovskii, P. Lecanda, R. Huerta, H. D. I. Abarbanel, and G. Laurent, "Dynamical encoding by networks of competing neuron groups: Winnerless competition," Physical Review Letters **87** (2001), 10.1103/physrevlett.87.068102.
[18]V. S. Afraimovich, V. P. Zhigulin, and M. I. Rabinovich, "On the origin of reproducible sequential activity in neural circuits," Chaos: An Interdisciplinary Journal of Nonlinear Science **14**, 1123–1129 (2004).
[19]S. H. Strogatz and R. M. Westervelt, "Predicted power laws for delayed switching of charge-density waves," Physical Review B **40**, 10501–10508 (1989).
[20]S. H. Strogatz, *Nonlinear Dynamics and Chaos: With Applications to Physics, Biology, Chemistry and Engineering* (Westview Press, 2000).
[21]A. N. Gorban, I. Tyukin, E. Steur, and H. Nijmeijer, "Lyapunov-like conditions of forward invariance and boundedness for a class of unstable systems," SIAM Journal on Control and Optimization **51**, 2306–2334 (2013).
[22]D. Sussillo and O. Barak, "Opening the Black Box: Low-Dimensional Dynamics in High-Dimensional Recurrent Neural Networks," Neural Computation **25**, 626–649 (2013), https://direct.mit.edu/neco/article-pdf/25/3/626/881886/neco_a_00409.pdf.
[23]M. I. Rabinovich, R. Huerta, and P. Varona, "Heteroclinic synchronization: Ultrasubharmonic locking," Physical Review Letters **96** (2006), 10.1103/physrevlett.96.014101.
[24]A. D. Horchler, K. A. Daltorio, H. J. Chiel, and R. D. Quinn, "Designing responsive pattern generators: stable heteroclinic channel cycles for modeling and control," Bioinspiration and Biomimetics **10**, 026001 (2015).
[25]M. W. Meeuse, Y. P. Hauser, L. J. M. Moya, G.-J. Hendriks, J. Eglinger, G. Bogaarts, C. Tsiairis, and H. Großhans, "Developmental function and state transitions of a gene expression oscillator in emphCaenorhabditis elegans," Molecular Systems Biology **16** (2020), 10.15252/msb.20209498.
[26]L. Jutras-Dubé, E. El-Sherif, and P. François, "Geometric models for robust encoding of dynamical information into embryonic patterns," eLife **9** (2020), 10.7554/elife.55778.
[27]S. Farjami, K. C. Sosa, J. H. P. Dawes, R. N. Kelsh, and A. Rocco, "Novel generic models for differentiating stem cells reveal oscillatory mechanisms," Journal of The Royal Society Interface **18** (2021), 10.1098/rsif.2021.0442.
[28]P. G. L. Sanchez, V. Mochulska, C. M. Denis, G. Mönke, T. Tomita, N. Tsuchida-Straeten, Y. Petersen, K. Sonnen, P. François, and A. Aulehla, "Arnold tongue entrainment reveals dynamical principles of the embryonic segmentation clock," eLife **11** (2022), 10.7554/elife.79575.
[29]S. Kato, H. S. Kaplan, T. Schrödel, S. Skora, T. H. Lindsay, E. Yemini, S. Lockery, and M. Zimmer, "Global brain dynamics embed the motor command sequence of caenorhabditis elegans," Cell **163**, 656–669 (2015).
[30]A. L. A. Nichols, T. Eichler, R. Latham, and M. Zimmer, "A global brain state underlies emphC. elegans sleep behavior," Science **356** (2017), 10.1126/science.aam6851.
[31]C. Langdon, M. Genkin, and T. A. Engel, "A unifying perspective on neural manifolds and circuits for cognition," Nature Reviews Neuroscience **24**, 363–377 (2023).
[32]M. Morrison and L.-S. Young, "Chaotic heteroclinic networks as models of switching behavior in biological systems," Chaos: An Interdisciplinary Journal of Nonlinear Science **32** (2022), 10.1063/5.0122184.
[33]P. beim Graben and A. Hutt, "Detecting Recurrence Domains of Dynamical Systems by Symbolic Dynamics," Phys. Rev. Lett. **110** (2013).
[34]F. Corson and E. D. Siggia, "Geometry, epistasis, and developmental patterning," Proceedings of the National Academy of Sciences **109**, 5568–5575 (2012).
[35]B. Ermentrout, *Simulating, Analyzing, and Animating Dynamical Systems* (Society for Industrial and Applied Mathematics, 2002).
[36]A. Dey and D. Barik, "Potential landscapes, bifurcations, and robustness of tristable networks," ACS Synthetic Biology **10**, 391–401 (2021).
[37]J. E. Ferrell and S. H. Ha, "Ultrasensitivity part iii: cascades, bistable switches, and oscillators," Trends in biochemical sciences **39**, 612–618 (2014).

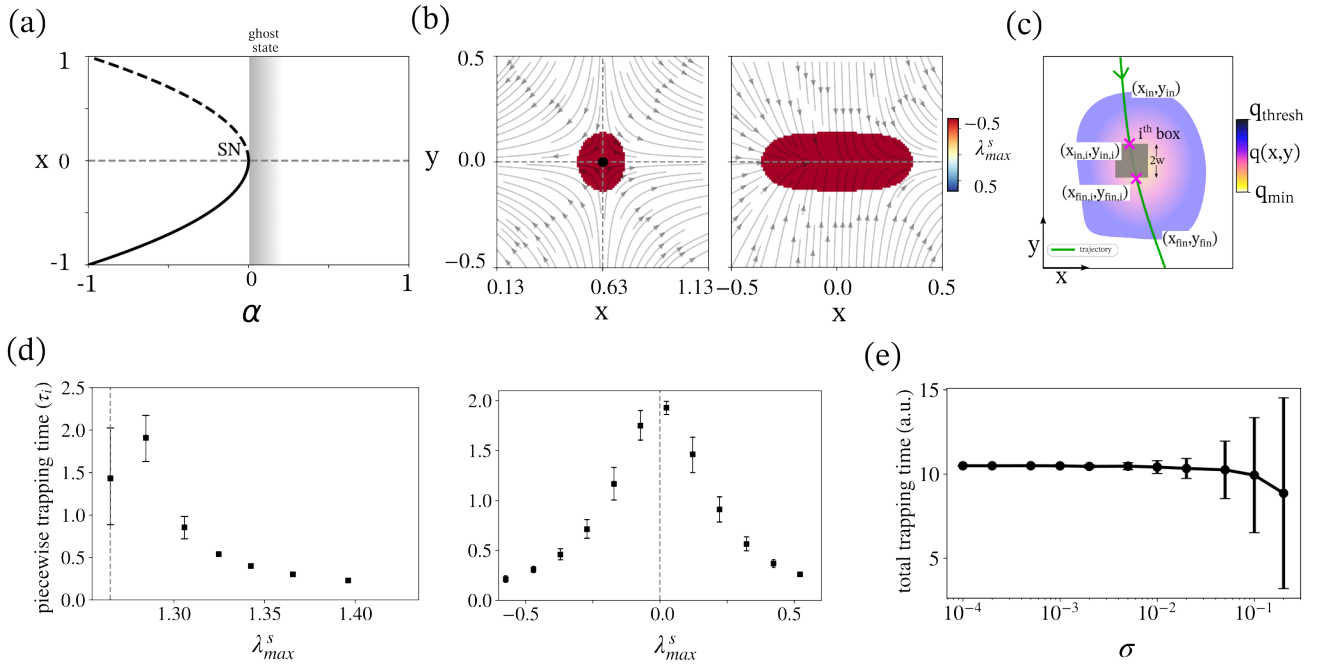

Supplementary Fig. 1 Characterization of the dynamics of saddle fixed points and ghost manifolds. (a) Bifurcation diagram corresponding to Eq. 1. Solid/dashed lines: stable/unstable fixed points. Gray shaded area: region of ghost state. SN: saddle-node bifurcation. (b) λ^s_{min} at the region of slow dynamics for the saddle fixed point (left) and the ghost state (right). Corresponding to Fig. 2(a),(b). (c) Schematic of the total/piece-wise trapping time estimation in the region of slow dynamics. Magenta crosses: entry and exit points of trajectory into the i^{th} box, (x_{in}, y_{in}) and (x_{fin}, y_{fin}) are the entry and exit points of trajectory in the region. (d) Dependence of the piece-wise trapping time on the λ^s_{max} for the saddle (left) and the ghost state (right). Mean ± s.d. from 10 realizations starting from different initial conditions is shown. (e) Total trapping time as a function of noise intensity σ for the supplementary single ghost model (Eq. 9). Mean ± s.d. from 30 realizations starting from different initial conditions are shown.

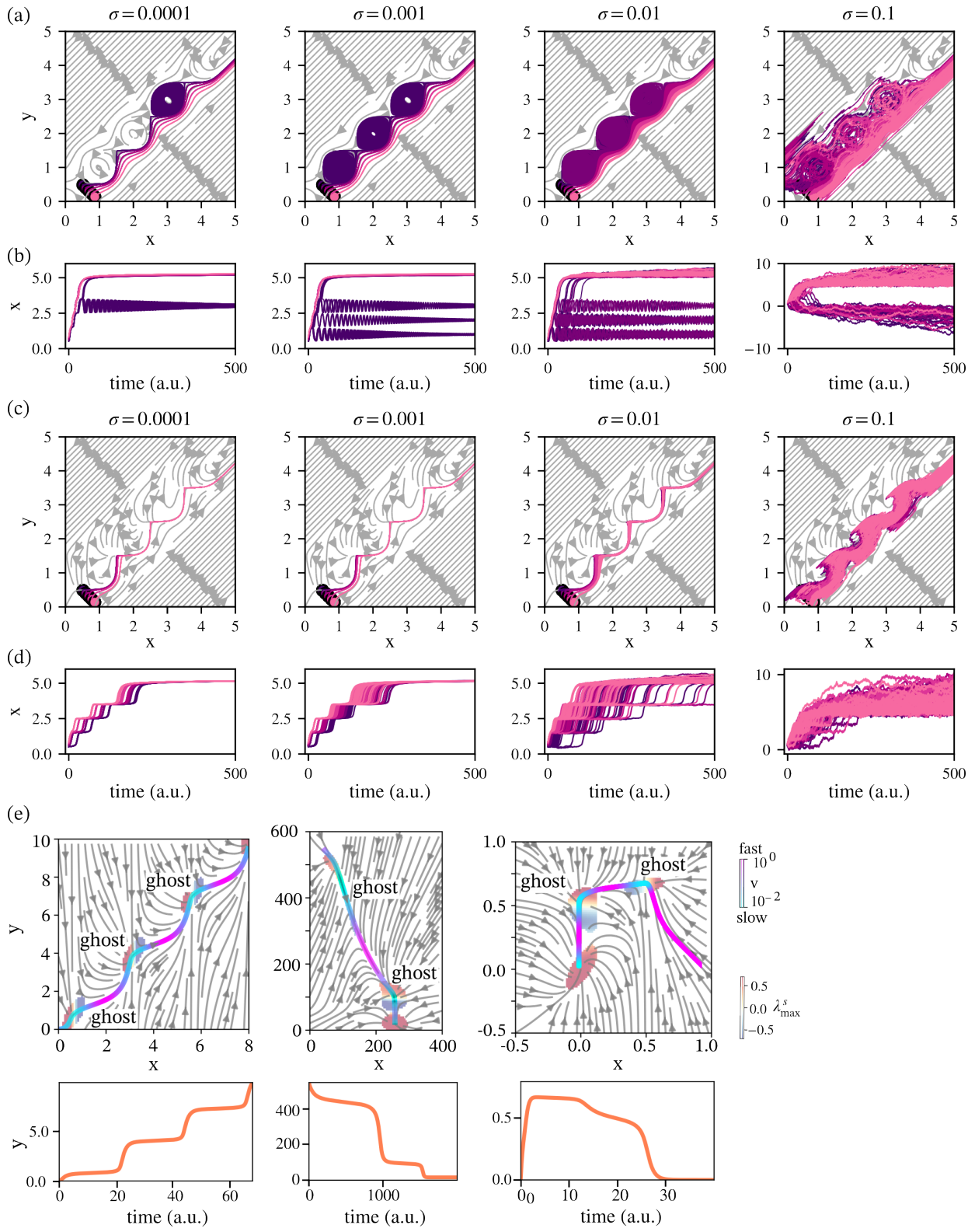

Supplementary Fig. 2 Dynamics of heteroclinic (HCh) and ghost (GCh) channels. (a) Exemplary phase space trajectories from different initial conditions and for different σ for a heteroclinic channel. (b) Corresponding time series of the sample trajectories. (c), (d) Same as in (a), (b) but for a ghost channel. See Supplementary materials section on 'Construction of generic heteroclinic/ghost channels' for more details. (e) Top: Phase space trajectories (color-coded by the velocity) and the numerical λ^s_{max} estimation at the regions of slow dynamics. Bottom: corresponding time series for models Eqs. 10, 11 and 12 (q_{thresh} = 0.2, 0.5, 0.007) from left to right. Corresponding to Fig. 3.

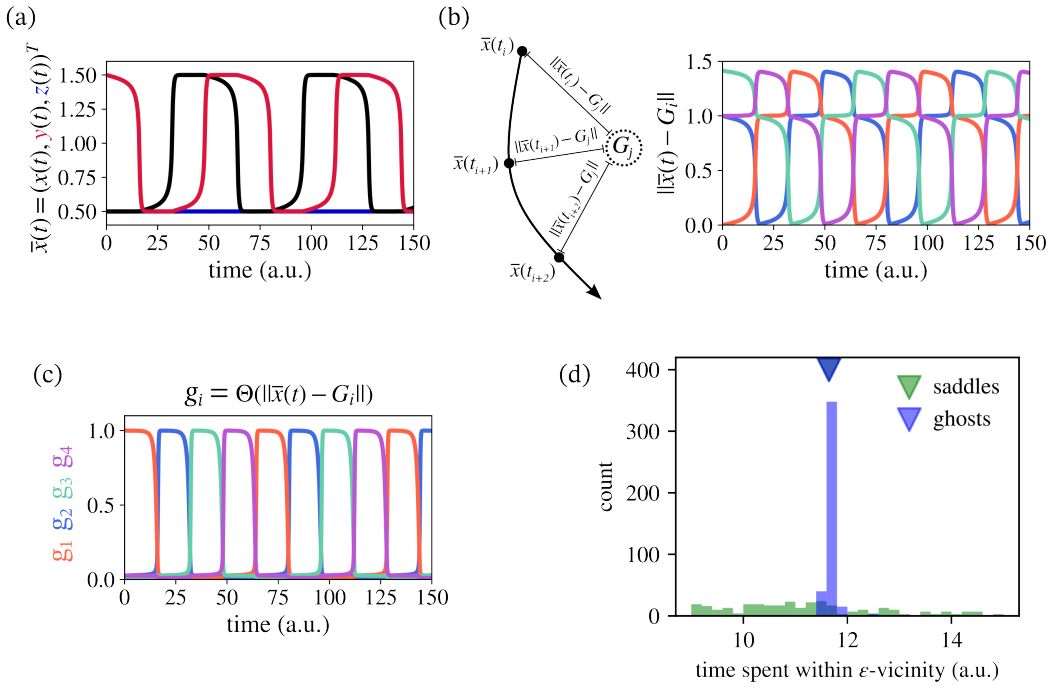

Supplementary Fig. 3 Characteristics of the shape of GC/HC oscillations and trapping times. (a) Time courses of the system variables for the ghost cycle (cf. section III.B). (b) Schematic and exemplary time series of Euclidean distances between each point in the trajectory to each of the ghost position. (c) Mapped distance time series using a Hill-type function Θ. (d) To conduct the comparative analyses between heteroclinic and ghost cycles starting from a similar baseline, the times spent within the vicinity of the ghost/saddle points were calculated and the saddle value was adjusted to minimize the differences of the average time spent in saddle/ghost vicinity (colored triangles) for the lowest noise level used in this work ($\sigma = 10^{-4}$). At $\nu = 4$, the difference between average trapping in saddle/ghost states reached $< 1\%$, which was thus used for all simulations of the HC.

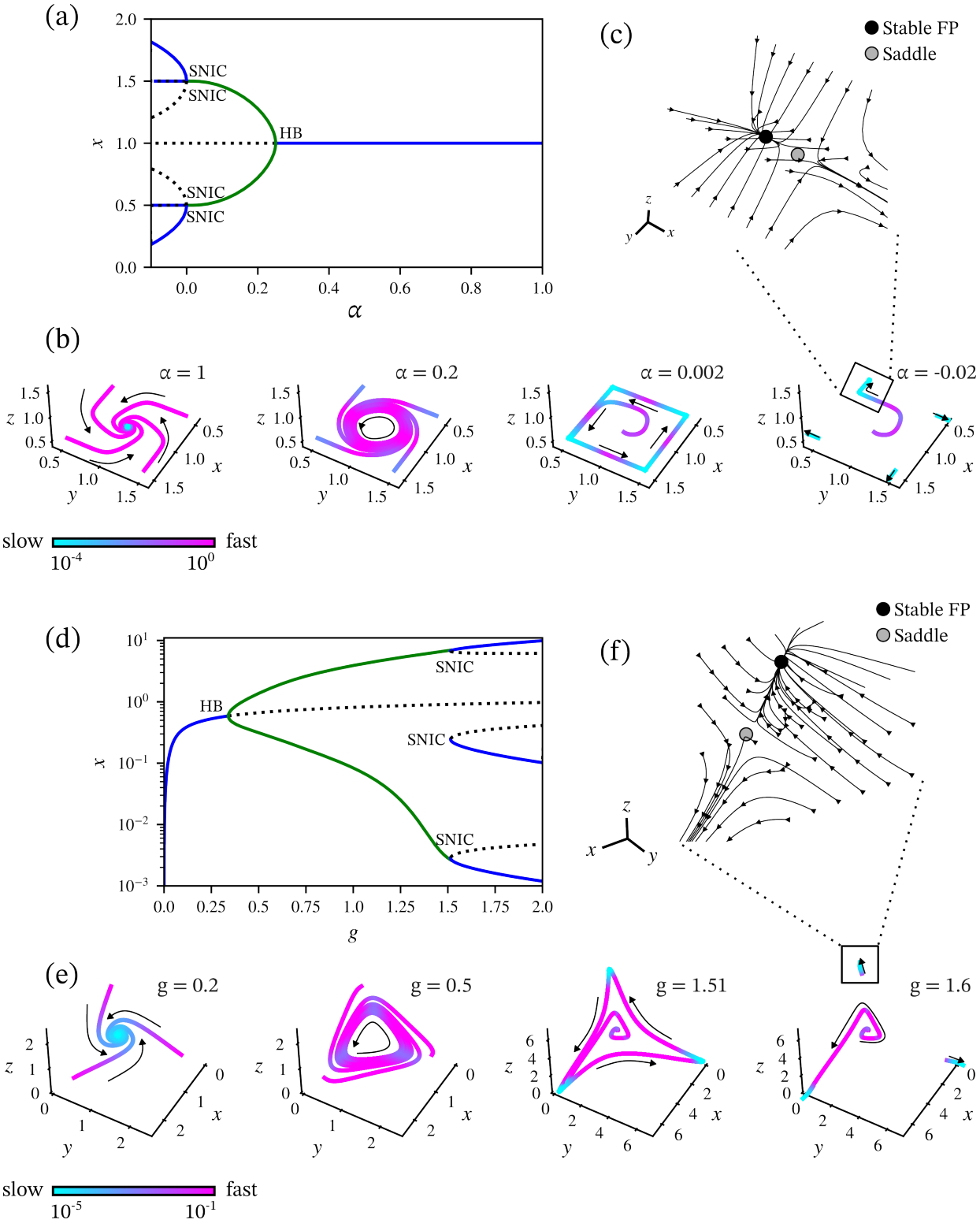

Supplementary Fig. 4 Mechanism of emergence of a ghost cycle. (a) Bifurcation diagram of ghost cycle described in section III.B. Blue/green lines: stable fixed point/limit cycle, dashed line: saddle fixed point. HB: Andronov-Hopf bifurcation, SNIC: saddle-node on infinite cycle bifurcation. (b) Phase space trajectories for different parameter values depicting the different dynamical regimes in (a), colour-coded by the speed in phase space. (c) Phase-space cut-out depicting the emergence of a stable fixed point and a saddle after the SNIC bifurcation. (d) Equivalent as in (a), only for the supplementary ghost cycle model, Eq. 14. Line description and notation as in (a). (e) Corresponding phase-space trajectories for different parameter values depicting the different dynamical regimes in (d). (f) Same as in (c), only for the model in (d).